Article

Investigating Permselectivity in PVDF Mixed Matrix Membranes Using Experimental Optimization, Machine Learning Segmentation, and Statistical Forecasting

Saketh Merugu, Logan T. Kearney, Jong K. Keum, Amit K. Naskar, Jamal Ansary, Aidan Herbert, Monsur Islam, Kunal Mondal, and Anju Gupta*

Cite This: ACS Omega 2024, 9, 28764−28775

Read Online

ACCESS | 📊 Metrics & More | 📖 Article Recommendations | 🆂🆘 Supporting Information

ABSTRACT: This research examines the correlation between interfacial characteristics and membrane distillation (MD) performance of copper oxide (Cu) nanoparticle-decorated electrospun carbon nanofibers (CNFs) polyvinylidene fluoride (PVDF) mixed matrix membranes. The membranes were fabricated by a bottom-up phase inversion method to incorporate a range of concentrations of CNF and Cu + CNF particles in the polymer matrix to tune the porosity, crystallinity, and wettability of the membranes. The resultant membranes were tested for their application in desalination by comparing the water vapor transport and salt rejection rates in the presence of Cu and CNF. Our results demonstrated a 64% increase in water vapor flux and a salt rejection rate of over 99.8% with just 1 wt % loading of Cu + CNF in the PVDF matrix. This was attributed to enhanced chemical heterogeneity, porosity, hydrophobicity, and crystallinity that was confirmed by electron microscopy, tensiometry, and scattering techniques. A machine learning segmentation model was trained on electron microscopy images to obtain the spatial distribution of pores in the membrane. An Autoregressive Integrated Moving Average with Explanatory Variable (ARIMAX) statistical time series model was trained on MD experimental data obtained for various membranes to forecast the membrane performance over an extended duration.
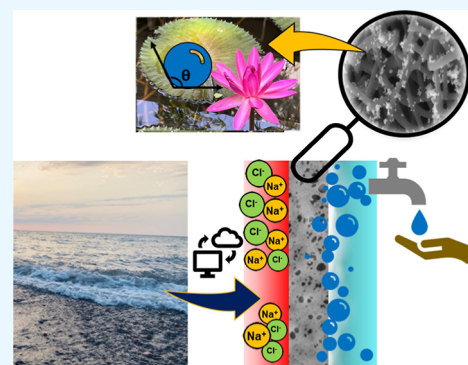
1. INTRODUCTION

Global water scarcity, exacerbated by population growth, climate change, and industrialization, is a pressing issue.[1] Despite 97% of Earth's water being seawater, only 0.06% of the total water is accessible freshwater. Efficient ocean water desalination is thus crucial.[2] The semiconductor industry's growing demand for high-purity water for silicon purification, wafer cleaning, and cooling systems further underscores this need.[3] Various membrane-based processes, including reverse osmosis, distillation, filtration, electrodialysis, and pervaporation, are being explored for energy-efficient water purification.[4−8] Membrane distillation (MD), a hybrid thermal and membrane process, is particularly promising due to its ability to handle high-concentration discharges, operate under low temperatures and pressures, resist fouling, and utilize renewable energy sources.[9−12] MD offers 50−75% energy efficiency, superior rejection rates, and cost-effective separations at $0.9/m³, compared to the average $2.92/m³ of other technologies.[13,14]

In MD, a hydrophobic polymer membrane separates nonvolatile and volatile components from wastewater. Membrane properties like pore diameter, porosity, thickness, mechanical strength, and interfacial characteristics can be adjusted to control water vapor transport and salt retention.[15−19] Hydrophobic membranes with antiwetting proper-

ties and thermal stability are preferred. Hydrophobic polymers like polypropylene, polytetrafluoroethylene, poly(vinylidene fluoride), and polysulfone are commonly used due to their strength, stability, and hydrophobicity. Polyvinylidene fluoride (PVDF) membranes are particularly notable for their chemical and thermal properties and their ability to promote microporosity.[20,21] Integrating nanomaterials into polymeric membranes can enhance their characteristics, leading to increased water vapor flux and salt retention, crucial for MD applications.[22−24] This can be achieved through surface coatings or by creating a mixed matrix with a polymer cast solution.[24,25]

In our recent studies, we enhanced boiling surfaces using coatings of graphene,[26] graphene oxide,[27] reduced graphene oxide,[28] graphene nanoplatelets,[29] and copper particles.[30] This led to a higher critical heat flux at lower surface temperatures due to enhanced thermal and interfacial properties.[20,21,23−25,31]
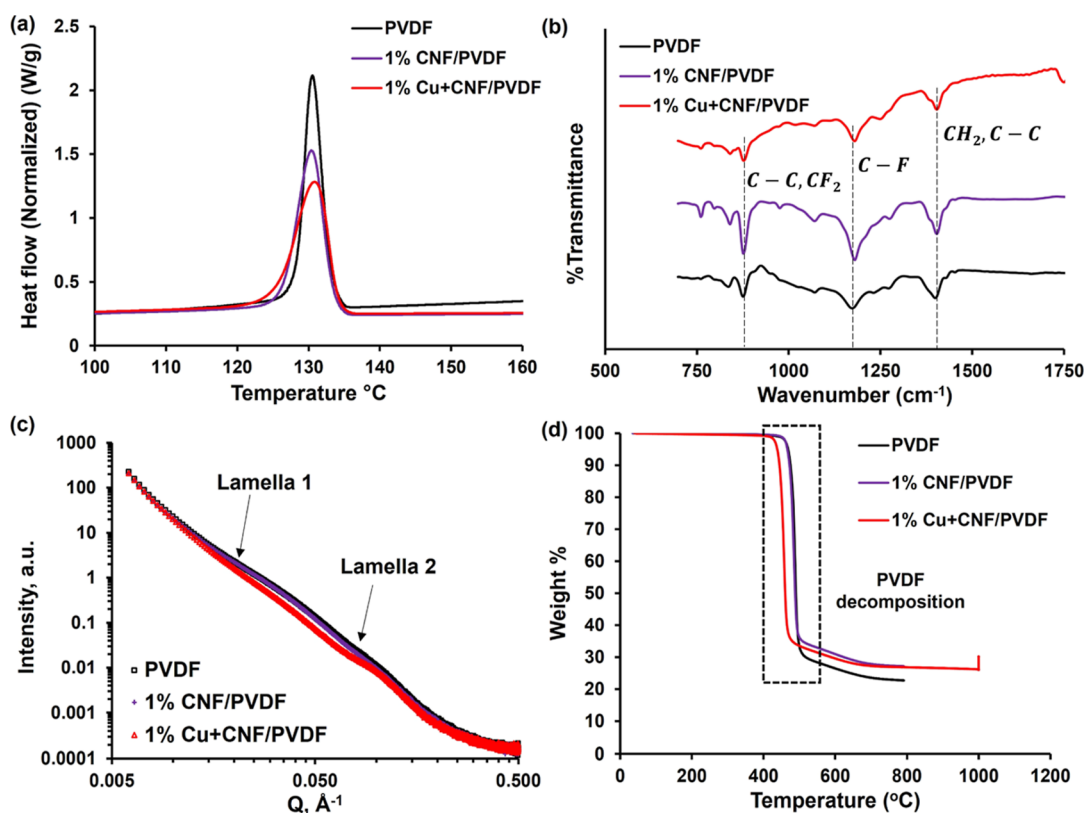
Figure 1. Comparison of properties of PVDF, CNF/PVDF, and Cu + CNF/PVDF membranes at 1 wt % (a) DSC curve demonstrating cold crystallization peak, (b) FTIR spectra with chemical functional and α crystal peaks, (c) SAXS analysis study, and (d) thermogravimetric analysis curve.

In thermally driven processes, the three-phase contact among liquid, vapor, and the heated solid surface is crucial for heat and mass transfer. Incorporating nanomaterials into membranes have been shown to improve permeate fluxes, fouling-resistance, and durability.[22,32,33] Recent studies have used nanomaterial modified PVDF membranes for MD applications, achieving superior water contact angles and fluxes. Wei et al. reported silver nanoparticle coated membranes with a water contact angle of 151.6 ± 2.5° and a flux of 17.6 kg m^{-2} h^{-1}.[33] Reddy et al. developed mixed matrix membranes of PVDF and TiO$_2$, demonstrating a vapor flux of 5.10 ± 0.10 kg m^{-2} h^{-1} and effective dye extraction from textile wastewater.[34] Yadav et al. developed SiO$_2$ modified PVDF nanofibrous membrane with a water contact angle of 154.6°, which produced a vapor flux of 11.5 kg m^{-2} h^{-1}.[35] Additionally, carbon based nanomaterials, such as reduced graphene oxide blended with PVDF membranes, resulted in 31.79% increase in vapor flux compared to pristine PVDF membrane,[36] and multiwall carbon nanotube spray coated PVDF membranes yielding a vapor flux of 33.2 kg m^{-2} h^{-1}.[37]

This study introduces copper-oxide-nanoparticle-impregnated carbon nanofibers (CNFs) incorporated into a PVDF polymer matrix via wet phase inversion. We hypothesized that Cu and CNF would induce chemical and morphological heterogeneity, leading to improved wettability, porosity, and pore dynamics for efficient MD. We investigated electrospun CNF/PVDF and Cu + CNF/PVDF mixed membranes, optimizing CNF and Cu concentrations for membrane wetting and pore dynamics. A comprehensive structure−property-performance correlation analysis was performed using physioch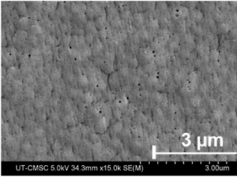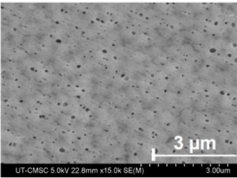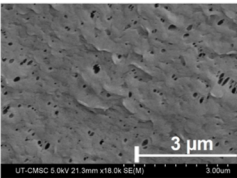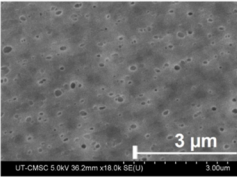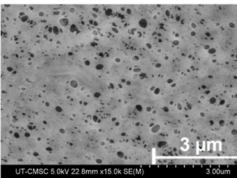emical, thermal, and mechanical analyses, along with small- and wide-angle X-ray scattering (SAXS and WAXS). A machine learning (ML) tool was used for scanning electron microscopy (SEM) micrograph image processing to determine spatial porosity. The Cu + CNF/PVDF membranes achieved the highest salt rejection and vapor flux due to superior interfacial properties. An autoregression model was trained on MD data for time series performance analysis.

2. RESULTS AND DISCUSSION

2.1. PVDF and Mixed Membrane Properties: Crystallinity and Thermal Stability. Crystallinity of membranes plays a crucial role in determining their MD performance. Enhanced crystallinity in polymer membranes typically results in reduced permeability due to decreased free volume, but it can improve selectivity due to a more ordered structure. Crystalline regions, being more thermally stable than amorphous ones, contribute to the membrane's thermal stability, a critical factor for high-temperature processes. Additionally, higher crystallinity augments the membrane's mechanical strength, thereby increasing its resistance to operational stresses. It also influences the membrane's surface properties, impacting its fouling resistance. Studies have also indicated that membranes with larger pore sizes, which are associated with higher crystallinity, exhibit reduced nucleation time and increased crystal growth rate.[38,39] Prior work analyzed variations in the crystalline conformation of PVDF chains in the PVDF/poly(methyl methacrylate) blends, where the degree of crystallinity and the molecular mobility in the amorphous phase were quantitatively estimated using the nuclear magnetic resonance spectroscopy.[40] PVDF has been reported to possess several crystalline polymorphs, such as α-,

Table 1. Scanning Electron Microscope Images and Effective Mean Pore Diameters of PVDF and CNF/Cu + CNF Mixed PVDF Membranes at 1 and 2 wt % Loading

Membrane	SEM	Effective Mean Pore Diameter (nm)
PVDF		93.5 Circular pores
1 wt% CNF/PVDF		114.4
1 wt% Cu+CNF/PVDF		128.2 Noncircular pores 37.3% ↑ compared to the PVDF membrane
2 wt% CNF/PVDF		128.4
2 wt% Cu+CNF/PVDF		247.4 Noncircular pores 164.6% ↑ compared to PVDF

β-, γ-, δ-, ε-, out of which α-, β-, and γ are the dominant conformations. α-Form crystallites are the most stable conformation in melt-crystallized PVDF and can be identified on IR spectra at 976, 855, 795, and 766 cm^{-1}.[41,42]

A comprehensive investigation of the crystallinity of PVDF membranes in the presence of Cu and CNF was performed using differential scanning calorimetry (DSC), Fourier transform infrared spectroscopy (FTIR), and SAXS. Figure 1a represents the cold crystallization DSC. All three membranes yielded a crystallization peak at around 130 °C; however, a significant difference in the shape and magnitude of these peaks were noted in the presence of multiscale CNF and Cu materials in the PVDF matrix. The integration of nanomateri-

als into the PVDF matrix serves as nucleation sites, promoting the crystallization of PVDF. The degree of crystallinity of PVDF membrane was around 0.37%, and with the integration of 1 wt % CNF and Cu + CNF, the degree of crystallinity increased to 0.39 and 0.4%. This behavior is widely reported to alter the thermal characteristics of PVDF, as evidenced by the broadening of the DSC peak.[43,44] In this study, CNF and Cu altered the formation of α crystal system but that the CNF and Cu nanoadditives moderate the formation of the ordered phase, likely through restricted mobility. The compatibility of the nanofillers and the PVDF polymer is critical for ensuring stability and performance of the mixed matrix membranes.[45−47] The thermodynamic compatibility of the polymer
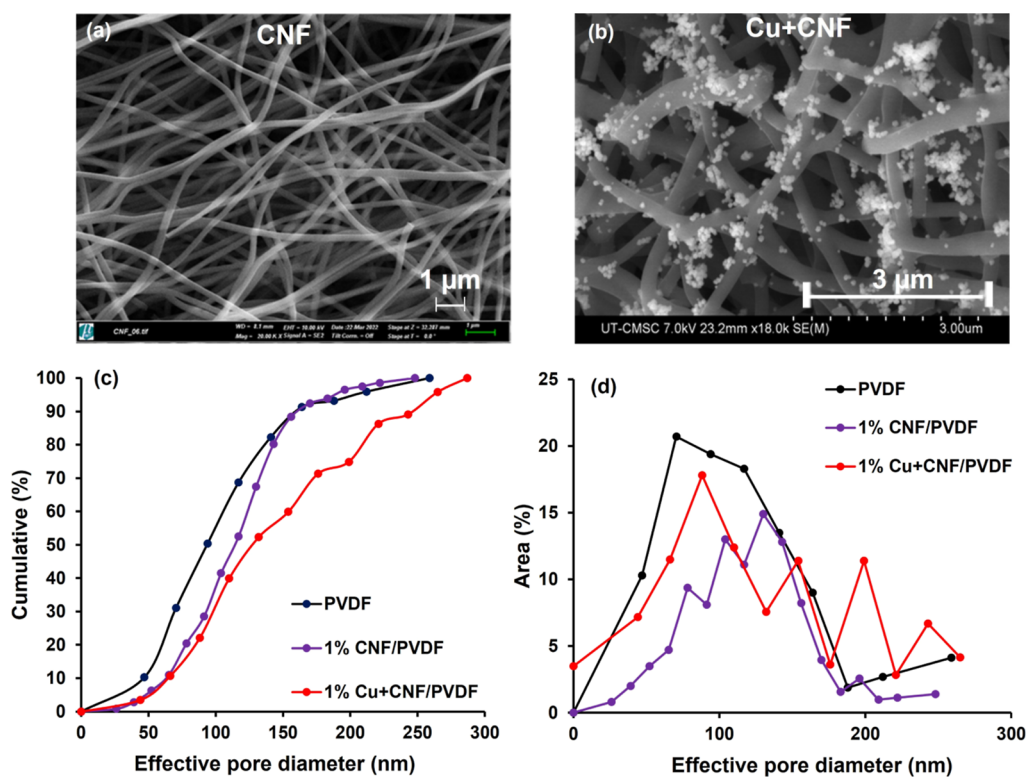
Figure 2. SEM images of (a) CNF, (b) CuO decorated CNF (Cu + CNF) and digiM I2S image analysis showing (c) cumulative % and (d) area % pore size distribution for PVDF, 1% CNF/PVDF, and 1% Cu + CNF/PVDF membranes.

and the nanoparticles dispersed in the polymer matrix was assessed using the Flory−Huggins interaction parameter given by equation.[48]

$$\chi = \frac{\Delta H_{mix}}{kT} \tag{1}$$
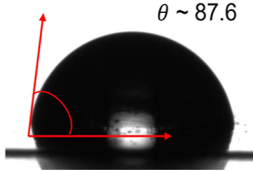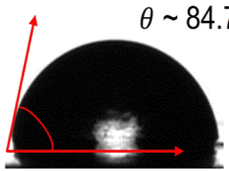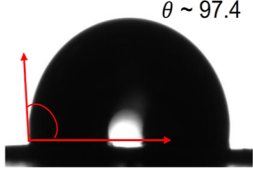
where χ is the Flory−Huggins interaction parameter, ΔH_{mix} is the enthalpy of mixing for the mixed matrix membrane calculated using eq S1 of Supporting Information, k is the Boltzmann constant, and T is the absolute temperature. The calculated Flory−Huggins interaction parameter for CNF/PVDF was ∼0.119 and ∼0.093 for the Cu + CNF/PVDF membrane. Both the mixed matrix membranes exhibited low (close to zero) Flory−Huggin's interactions parameters, indicating good thermodynamic compatibility and stability between polymer and nanofiller.[49,50]

Figure 1b compares the FTIR spectra of PVDF, CNF/PVDF, and Cu + CNF/PVDF at 1 wt % Cu and CNF with respect to PVDF. For all the membranes, strong absorption bands for antisymmetric C−C stretching and symmetric CF_2 stretching vibration were observed at 875 cm^{-1}, asymmetrical C−F stretching peak was observed at 1178 cm^{-1}, and CH_2 wagging vibration along with antisymmetric C−C stretching vibration was observed at 1405 cm^{-1}, native to PVDF polymers.[51,52] The bands around 750 cm^{-1} observed in FTIR spectra can also be attributed to the presence of α crystals.[40,41] X-ray Scattering (XS) measurements were performed on the membrane films to further elucidate the morphological details within the films further. WAXS data revealed commonly reported α and β peak structures with negligible differences between the membrane formulations (Figure S1). However, subtle differences appear in the SAXS data shown in Figure 1c, with an unambiguous reduction in the

first lamellar feature ($q \sim 0.04$) in the system containing Cu particles. This result is consistent with a reduction in density-driven contrast, or reduced order, resulting from the frustrated chain diffusion at the crystal growth face.[53] While the SAXS data strongly suggest the presence of two distinct lamellar structures in the mixed matrix membranes, direct morphological evidence is lacking. Future work will involve complementary techniques such as transmission electron microscopy or atomic force microscopy to visually confirm and investigate the lamellar morphology observed through SAXS analysis. The membranes were tested for their stability within the operating temperature range of MD and at higher temperatures for their potential future applications in high temperature gas separation. Figure 1d compares the dynamic thermogravimetric curves of the membranes that demonstrate their stability up to 400 °C.

2.2. Pore Morphology, Porosity, and Wetting Characteristics of PVDF and Mixed Matrix Membranes. Table 1 summarizes the SEM images of PVDF and mixed matrix membranes with 1 and 2 wt % CNF and Cu + CNF. Several other lower and higher concentrations of CNF and Cu + CNF were also investigated to elucidate their effect on overall membrane properties. The thickness of the fabricated membranes was in the range 50 ± 4 μm measured using a micrometer. Brunauer−Emmett−Teller (BET) analysis was performed to report the porosity of the membranes and is presented in Supporting Information Figure S2. The effective pore diameters and % pore size distributions of the membranes computed using digiM I2S image analysis are summarized in Table 1 and in Supporting Information Figure S3, respectively. The mean pore diameter of the PVDF membranes obtained was 93.5 nm. The pore diameters increased with increasing CNF and Cu + CNF loading. The average pore diameter of 1

Table 2. Comparison of Static and Dynamic Contact Angle of PVDF and 1 wt % CNF/PVDF, 1 wt % Cu + CNF/PVDF Mixed Membranes

Membrane	ACA (°)	RCA (°)	Hysteresis (°)	Static Water Contact Angle (°)
PVDF	95.3±1.5	48.6±13	46.6	θ ~ 87.6
CNF/PVDF	91.7±1.1	39.8±5	51.9	θ ~ 84.7
Cu+ CNF/PVDF	95.7±2.4	41.5±10.4	54.1	θ ~ 97.4

wt % CNF/PVDF was greater by 22.3%, and 2 wt % CNF loading further increased by 37.1% compared to the PVDF membrane's mean pore diameter. Additionally, copper nanoparticle decorated CNFs increased the mean pore size of the mixed matrix membranes by 37.1% for 1 wt % loading and 165% for 2 wt % loading. The increase in pore diameters can be attributed to the presence of CNF and Cu + CNF in the polymer matrix, resulting in instantaneous demixing and macrovoid formation.[54]

In PVDF membranes, the shape of pores was observed to deviate from the typical circular form when CNFs and copper (Cu) nanoparticle-decorated CNFs were introduced. Instead of circular pores, ellipsoidal or elongated pores emerged. This noncircularity arises from heterogeneity in the polymer matrix during the phase inversion process, a phenomenon supported by similar findings in existing literature.[38−40] The underlying mechanisms involve nanoconfinement effects and geometric packing constraints, which limit the available free space within the polymer chains and impact the overall membrane structure. The influence of high surface energy from multidimensional nanomaterials (such as nanofibers and nanoparticles) further contributes to this deviation from circularity. The local arrangement of polymer chains is altered due to the presence of these nanomaterials.[55−57] Figure 2a,b depict SEM images of electrospun CNFs and Cu nanoparticle-decorated CNFs, respectively. The electrospinning process yielded uniform-diameter CNFs with diameters ranging from 1.2 to 1.6 nm. Subsequent single-step thermal reduction with a copper salt solution resulted in a homogeneous distribution of copper particles within an interwoven CNF network. The addition of Cu particles modified the surface properties, creating energeti-

cally favored sites that potentially influenced the overall pore shape.

Figure 2c,d compare the effective pore size distribution of PVDF and 1 wt % CNF and Cu + CNF/PVDF mixed membranes by applying ML segmentation to SEM images shown in Table 1. The analyses for higher concentrations of Cu and CNF are presented in Supporting Information Figure S3. The integration of CNF led to a notable expansion in the pore size distribution peak due to their high surface area to volume ratio and distinct morphological features, that potentially created new pathways or modified the existing ones within the PVDF matrix. The heterogeneity introduced by CNF led to broadening of the pore size distribution. The porosity of PVDF membranes was found to be 2.7% where in the presence of CNF, the porosity was recorded to be 5.4%. However, upon addition of Cu nanoparticle-decorated CNFs, the porosity slightly dropped to 4.6%. The addition of nanofiber and nanoparticles can have different effects on its porosity due to their distinct morphologies and interactions with the polymer matrix. When nanofibers are added to the polymer membrane, they can create new void spaces or pores due to their elongated shape and large aspect ratio. These fibers can align themselves in a way that creates interconnected channels, thereby increasing the overall porosity of the membrane.[58] However, when Cu nanoparticles are subsequently added to CNFs, the situation changes. Nanoparticles, due to their small size and high surface area, have a strong tendency to aggregate.[59] When these aggregated nanoparticles are incorporated into the polymer-nanofiber matrix, they can fill the void spaces or pores created by the nanofibers, leading to a decrease in porosity. Moreover, nanoparticles can also
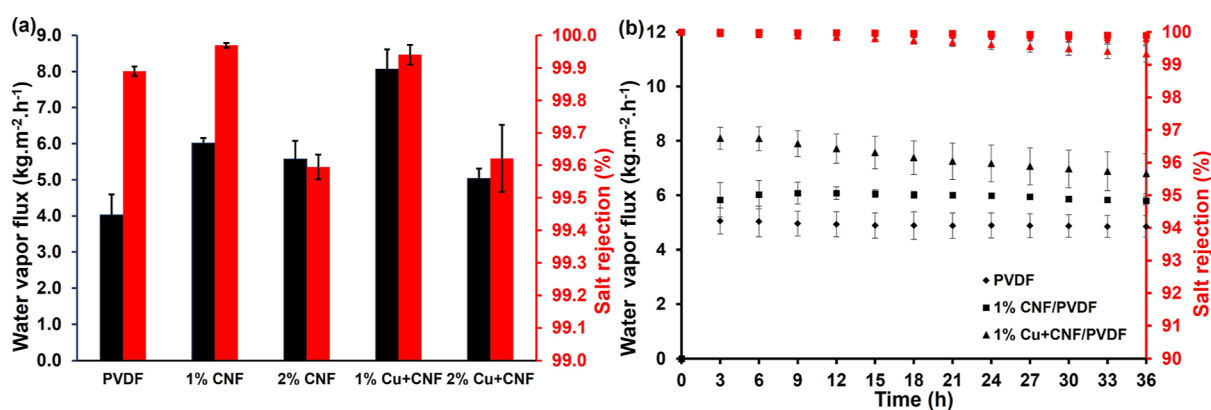
Figure 3. Water vapor flux and salt rejection plots (a) 1 and 2 wt % PVDF and mixed membranes for 10 h MD runs, (b) 36 h MD run for PVDF, 1 wt % CNF/PVDF, and 1 wt % Cu + CNF/PVDF membranes.

interact with the polymer chains and cause them to rearrange or compact around the particles, further reducing the pore volume. This phenomenon is often referred to as "polymer densification".[60,61] The addition of 2 wt % Cu + CNF increased the porosity, highlighting the significance of tuning the mixed membrane composition for desired properties. While this study employed ML segmentation for pore size characterization, the future work will involve modeling the transport of solute in heterogeneous porous media using a nonlinear convection-dispersion partial differential equation system developed by Michaels et al. (1980)[62] to obtain insights into the pore size distributions and effective pore diameters by analyzing the solute transport behavior through the porous material. Combining the ML segmentation approach with the solute transport method would allow for a more robust characterization of the porous structure. While ML segmentation can quantify pore sizes from imaging data, the solute transport method can complement this by probing the interconnectivity and tortuosity of the pore network, which are crucial factors influencing the effective pore diameters and overall transport properties.

Additionally, the incorporation of CNFs and copper-decorated CNFs (Cu + CNFs) into the mixed matrix membranes exhibited a modest enhancement in mechanical strength, as illustrated in Figure S5 of the Supporting Information. These improvements in mechanical properties can potentially be attributed to the influence of CNFs on the membrane's interfacial porosity and pore morphology.

The correlation between pore diameter and modified wetting characteristics of PVDF membrane upon addition of 1 wt % CNF and Cu + CNF was demonstrated by comparing the static and advancing contact angles. PVDF membranes yielded static contact angle (SCA) of 87.6° and advancing contact angle (ACA) of 95.3 ± 1.5° this is attributed to the cohesive forces within deionized water used for measurement that was stronger than the adhesive forces between the water and the PDVF membrane leading to a high contact angle and poor wetting. When incorporated with CNF, both SCA and receding contact angle decreased to 84.7° and 91.7 ± 1.1°, respectively. This slight alteration in contact angles with notable hysteresis presented in Table 2 is attributed to the combined effects of pore diameter and hydrophilicity induced by CNF in PVDF matrix according to the Washburn equation.[63]

$$\cos\theta = \frac{dp}{4\gamma} \tag{2}$$

where θ is the contact angle (deg) between the mercury and the membrane, d is the pore diameter (nm), p is the applied pressure (Pa), and γ is the surface tension of mercury (480 N/m). However, upon addition of Cu particles in CNF and PVDF matrix, the SCA significantly increased to 97.4°, while ACA increased to 95.7 ± 2.4 in the similar range of PVDF membrane. Contact angle hysteresis representing the difference between the advancing and receding contact angles was recorded highest for distilled water droplet on Cu + CNF/PVDF membranes, confirming the chemical and physical heterogeneity of membrane surfaces that arises from the pinning of contact angle line. Additionally, the water penetrated the membrane pores during the advancing phase and remained entrapped during the receding phase, leading to hysteresis. The changes in dynamic contact angles of the membranes with respect to time have been reported in Figure S4 of the Supporting Information. The surface roughness of PVDF and mixed matrix membranes was measured and reported in Table S2 of Supporting Information. The surface roughness of the mixed matrix membranes was higher than PVDF membranes, especially in the case of Cu + CNF mixed matrix membranes. The increase in SCA in the case of Cu + CNF membrane can be attributed to the increase in surface roughness.[64]

2.3. Experimental and Time Series Forecasting of PVDF and Mixed Matrix Membrane Desalination. PVDF, CNF, and Cu + CNF mixed PVDF membranes at 1 and 2 wt % concentrations were tested for their applications in using a direct contact membrane distillation (DCMD) module, specifically designed for this purpose. Throughout the MD experiment, the feed and permeate temperatures, feed concentrations, and flow rates of feed and permeate were kept constant. Figure 3a summarizes the water vapor flux and salt rejection rates obtained for CNF/PVDF and Cu + CNF/PVDF membranes over 10 h, respectively. The PVDF membranes exhibited a salt rejection of 99.89% but with a low water vapor flux of 4.03 kg m^{-2} h^{-1}. The salt rejection rate obtained for 1 wt % CNF was nearly 99.97% while with 2 wt % CNF it dropped slightly to 99.6% which was lower than that of PVDF membranes alone. Similarly, water vapor flux for 1 wt % CNF was obtained as 6 kg m^{-2} h^{-1} that slightly dropped to 5.6 kg m^{-2} h^{-1} with 2 wt % CNF, but still 39% higher than that yielded by PVDF membranes. Upon addition of 1 wt % Cu +
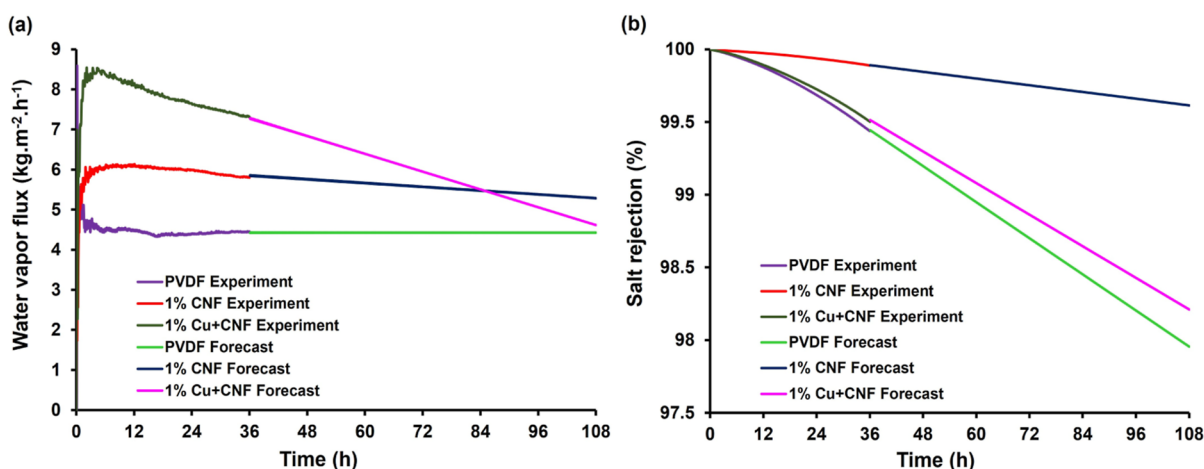
Figure 4. ARIMAX ML forecasting of fabricated membrane stability: (a) water vapor flux and (b) salt rejection.

CNF, the water vapor flux increased to 8.1 kg m^{-2} h^{-1} with a salt rejection rate of 99.94%, however, with 2 wt % Cu + CNF particles, the water vapor flux dropped significantly to 5.03 kg m^{-2} h^{-1} with a slight decline in salt rejection rate of 99.62%. The high performance achieved by 1 wt % Cu + CNF mixed membranes compared to PVDF membranes demonstrates a 101% increase in water vapor flux.

The high-water vapor flux is attributed to the increased porosity and modified pore size distribution by addition of 1 wt % Cu and CNF provided interfacial pathways for water vapor transport. However, an even higher porosity generated by 2 wt % led to a significant drop in water vapor flux that warrants further investigation. The presence of both CNF and Cu increases the surface roughness, as evident by high contact angle hysteresis that led to enhanced hydrophobicity that improved salt rejection rates by preventing the penetration of saltwater into the pores. Thus, achieving an optimal MD performance for desalination requires a fine balance between permeability and selectivity. While high porosity and pore diameter may improve flux, they may compromise selectivity.[65,66]

The water vapor flux for 1 wt % Cu + CNF/PVDF mixed membranes was observed to be significantly superior compared to 1 wt % CNF/PVDF and PVDF membranes, despite a marginal decrease over time. All the membranes exhibited a salt rejection rate of approximately 99.98%, although a reduction in this rate was noted for PVDF membranes, and a minor decline was observed for 1 wt % CNF membranes over a period of 36 h. Given the largely uncharted stability of nanomaterial-incorporated mixed membranes over prolonged durations, primarily due to the time-consuming and labor-intensive nature of MD experiments,[54−57] a time-series forecasting model was trained based on the experimental data gathered from 36 h runs. Autoregressive Integrated Moving Average with Explanatory Variable (ARIMAX) model was adopted to predict the salt rejection and water vapor flux for 108 h based on 36 h experimental data in Figure 3b. The details of the training steps are provided in Supporting Information Table S3 and Figure S6. The ARIMAX model is a versatile tool for predicting time series behavior while considering exogenous variables such as membrane properties, operating conditions, or other relevant parameters. The model chosen was based on its ability to forecast MD performance

while providing valuable insights on process optimization and nanomaterial selection.

The water vapor flux and salt rejection rate forecasts of PVDF, 1 wt % CNF, and 1 wt % % Cu + CNF PVDF membranes are demonstrated in Figure 4a,b, respectively. The PVDF membrane demonstrated a low, stable vapor flux of 4.4 ± 0.2 kg m^{-2} h^{-1} with decreasing salt rejection reaching 97.75% at 108 h. The 1% CNF exhibited a slightly higher and stable water vapor flux of 5.2 ± 0.3 kg m^{-2} h^{-1} with a high and stable salt rejection of 99.8% at 108 h. The 1% Cu + CNF initially exhibited high water vapor flux but decreased gradually, reaching 4.6 ± 0.1 kg m^{-2} h^{-1} with a low salt rejection close to 98.2% after 108 h, which may be due to the increased heat loss across the membranes due to the addition of Cu nanoparticles. Based on the forecasts, the 1% CNF demonstrated stable water vapor flux with high salt rejection over longer duration MD runs. Recent advancements in data training and predictive analysis techniques provide an opportunity to create experimentally informed models. These models can effectively forecast membrane performance and flux over extended operational periods. By adopting such approaches, MD processes can be optimized based on process parameters and membrane design to develop efficient membrane cleaning procedures that will ultimately enable prolonged membrane reuse.

3. CONCLUSIONS

Processes involving liquid−vapor phase change mechanisms such as MD rely on a solid−liquid interface with superior interfacial characteristics such as porosity, wettability, surface tension, and adsorption. Quantifying water vapor flux and salt rejection rates is intrinsic to optimizing desalination performance using mixed MD. This study highlights the role of multidimensional copper nano particles and CNFs incorporated in PVDF membranes to improve their permselectivity via porosity, crystallinity, and wettability. This presence of 1 wt % Cu/CNF at the water-PVDF membrane interface induced chemical heterogeneity, surface area, contact angle hysteresis, and hierarchical morphologies that provided a pathway for water vapor escape recording a 64% increase in water vapor flux compared to PVDF membranes at 99.9% salt rejection rate. The experimentally informed ML segmented image processing and statistical time series models from this study could pave the way for making data-driven decisions in
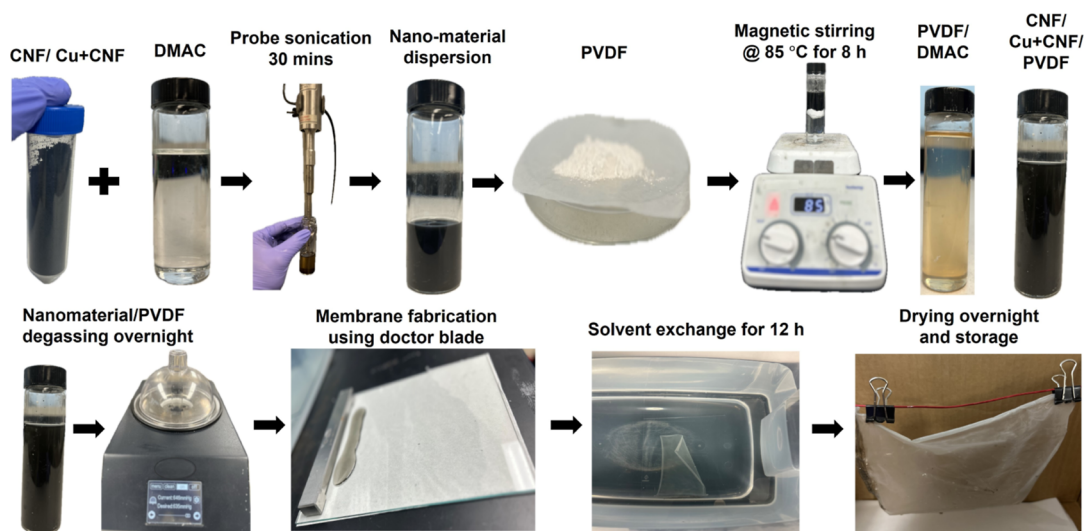
Figure 5. Schematic of the membrane fabrication process.

membrane design, stability, and operation. Future work could focus on optimizing the concentration of Cu and CNF particles in the PVDF matrix to further enhance membrane performance as well as exploring other potential applications of these mixed matrix membranes in high temperature gas separation processes.

4. MATERIALS AND EXPERIMENTAL METHODS

4.1. Materials. *N,N*-Dimethylacetamide (DMAc), poly-(vinylidene fluoride) polymer powder (MW—534,000), NaCl salt, and copper(II) acetate (Cu (OAc)$_2$), 1-heptanol were purchased from Sigma-Aldrich, USA. Deionized water with a conductivity of 2 μS/cm was utilized for all the experiments. CNF were gift samples from Karlsruhe Institute of Technology, Germany.

4.2. Fabrication of PVDF and Mixed Matrix Membranes. CNF were manufactured from the electro-spun polyacrylonitrile nanofibers via pyrolysis at 900 °C in an inert atmosphere as reported earlier.[67] A one step coating method was adopted to grow Cu nanoparticles on CNFs. 0.073 g of (Cu (OAc)$_2$) salt was dissolved in 20 mL of 1-heptanol by stirring mildly at 65 °C for 15 h to prepare a 20 mM supernatant Cu precursor solution.[68] The CNFs were added to a crucible containing Cu precursor solution and heated at 120 °C for 1 h in a vacuum oven to thermally grow copper oxide (CuO) nanoparticles as follows

$$Cu(CH_3COO)_2 \ (s) \xrightarrow[\text{1-Heptanol}]{T=120\ °C} CuO \ (s) + 2CH_3COOH$$
$$(3)$$
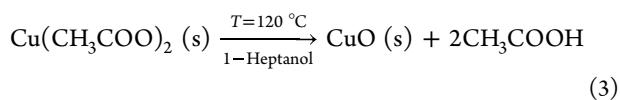
The PVDF, CNF/PVDF, and Cu + CNF/PVDF were synthesized via phase inversion technique by suspending 16 wt % PVDF pellets in DMAc solvent as shown in Figure 5. The resultant casting solution was gently heated at 85 °C for 8 h in a clear glass bottle under constant stirring until the homogeneous solution was obtained, which was then degassed overnight at room temperature. To synthesize the PVDF/CNFs modified nanocomposite membranes with 0.5, 1, and 2 wt % CNF content, the following protocol was followed.

First, an applicable quantity of CNFs with an average diameter of 175 nm were added to a certain volume of DMAc solvent and sonicated at 25−30 °C for at least 30 min to assist

the dispersal of the CNFs into the solvent matrix. About 2 g of PVDF polymer powder was added to the CNFs dispersion. The volume of CNF dispersion being added to PVDF powder was varied to prepare CNF/PVDF mixed matrix membranes with two different CNF loadings (1 and 2 wt % of PVDF polymer). These mixtures were heated to 80−90 °C, stirred for 6−8 h to get a homogeneous nanopolymer matrix, and then kept overnight for degassing. The resultant nanofiller/PVDF solution was cast on a glass plate with a thickness of 50 μm using a doctor blade; the membrane was allowed to dry, and the solvent was vaporized in the air for 30 s and directly submerged in deionized water at ambient temperature. The membranes were left in the water bath for 12 h for complete phase inversion, and then, the synthesized membranes were washed using deionized water, dried completely, and kept in a dry place. The same protocol was followed with Cu + CNFs to prepare the Cu + CNF/PVDF mixed matrix nanocomposite membranes.

4.3. Physiochemical and Thermal Characterization of PVDF and Mixed Matrix Membranes. Prior to imaging, PVDF, CNF/PVDF and Cu + CNF/PVDF membranes were sputter coated with gold. A HITACHI S-4800 high resolution SEM instrument at an accelerated voltage of 20 kV using both secondary electrons and backscattered electron detectors was utilized. The membrane thickness was confirmed using a micrometer and by examining the cross-section of the membrane via the SEM stage tilting. Elemental analysis (not shown) confirmed the presence of Cu on the membranes. The digiM I2S,[69] a ML semantic segmentation based image processing tool was used to identify the porous and polymeric regions on the SEM images. The first step involved supervised training of manually identifying the visible material, followed by training a cloud based artificial intelligence model on those identified pixels that are then generalized for the entire image. Post segmentation, the spatial distribution of pores was investigated using the method.

DSC measurements were performed between 25 to 180 °C at a rate of 10 °C/min in inert atmosphere on TA Instruments Q2500. FTIR with microattenuated total reflection (micro-ATR) was performed using Varian Excalibur Series FTS 4000 to verify the chemical bonds, their positions, shapes, and intensities of the components. The physical structure of the
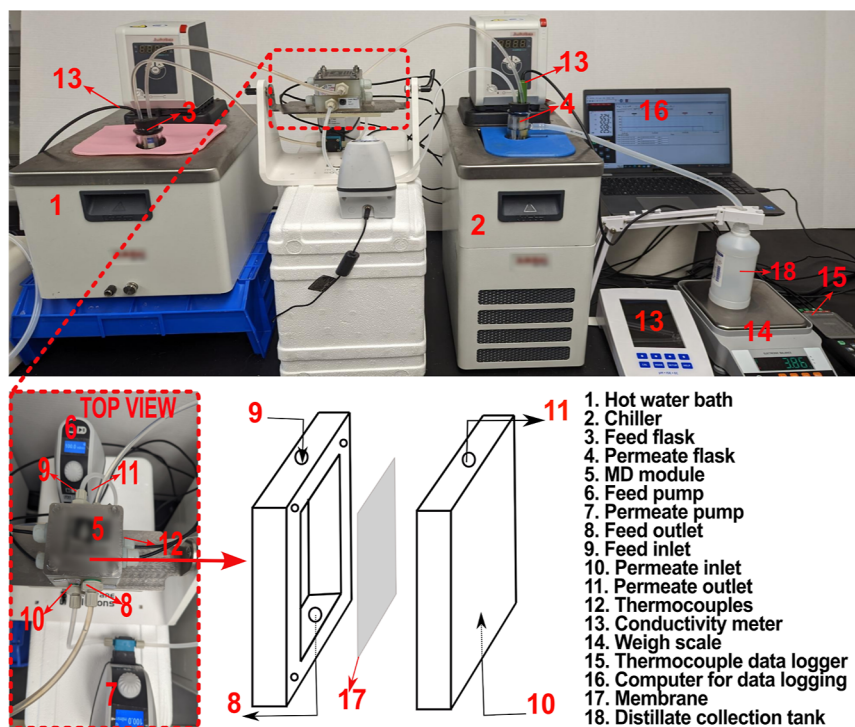
Figure 6. Custom designed MD test setup.

PVDF-based membranes was studied using a Xeuss 3.0 (Xenocs, France) XS instrument equipped with a D2+ MetalJet X-ray source (Ga Kα, 9.2 keV, λ = 1.3414 Å). Membrane sections were fixed to a solid sample holder and measured in transmission mode for 10 min at sample-to-detector distances of 47 mm (wide angle, WAXS) and 900 mm (small angle, SAXS). 2D images of the scattering patterns were collected on an Eiger 2R 4 M hybrid photon counting detector with a pixel dimension of 75 × 75 μm^2 (Dectris, Switzerland). The 2D SAXS images were circularly averaged and reduced in the form of absolute intensity versus scattering vector

$$q = \frac{4\pi \sin \theta}{\lambda} \tag{4}$$

The direct beam intensity was used to calibrate the measured intensities of each sample following background subtraction, and transmission corrections were applied in the XSACT software package (Xenocs, France). A multicomponent lamellar model was applied to fit the SAXS data to extract relevant physical parameters due to changes to the membrane formulations. Thermal stability of the membranes within MD operating temperatures were examined by using a TA Instruments Q50 Thermogravimetric Analyzer. The membrane samples were heated between 25 and 800 °C at a rate of 10 °C/min in inert atmosphere in hermetically sealed pans. Advancing and receding contact angles of the membranes were measured using a Theta Lite Optical Tensiometer by dispensing distilled water at a volume rate of 0.5 μL/s for 60 s.

4.4. MD Setup. Figure 6 is a photographic representation of the lab scale DCMD setup used in this study. The setup includes a hot water bath and chiller, feed and permeate tanks, an MD module with a 4 cm² effective area and 4 mm channel height (Solar Spring, Membrane Solutions, Germany), a data acquisition computer, two dosing pumps, a conductivity meter (HI5321-01, USA), a weight balance, and a thermocouple data

logger. The feed tank contained a 3.5 wt % NaCl solution, while the permeate tank held deionized water. The hot (70 °C) and cold (20 °C) streams, separated by the fabricated membranes inside the MD module, were circulated to maintain 100 mL/min crossflow rate. Permeate overflow was collected for durations dependent on the study, e.g., 10 h for performance testing and 36 h for stability tests. The conductivity of the permeate was measured using a meter in the permeate tank, and distillate weight was measured using a balance. Inlet and outlet temperatures of the feed and permeate streams, permeate conductivity, and permeate weight were logged. The experimental water vapor flux J_v across the membrane is usually expressed as

$$J_v = \frac{\Delta m}{At} \tag{5}$$

where Δm (kg) is the difference between the final and initial mass of the distillate, A the active membrane surface area (m²), t (h) is the MD operation time. The separation of nonvolatile components dissolved in the feed in MD is quantified by membrane separation efficiency

$$R\ (\%) = \left(1 - \frac{C_p}{C_f}\right) \times 100 \tag{6}$$

where, c_p and c_f are the concentrations (conductivities in our case) of the permeate and the feed solutions, respectively.

■ ASSOCIATED CONTENT

ⓢ Supporting Information

The Supporting Information is available free of charge at https://pubs.acs.org/doi/10.1021/acsomega.4c03024.

> Crystallinity analysis by WAXS, BET porosity analysis, ML segmentation for porosity by digiM I2S SEM image analysis, contact angle measurements for 2 wt % Cu and

CNF mixed PVDF membranes, tensile strength measurement of PVDF mixed membranes, and ARIMAX forecasting model: data set training and testing (PDF)

AUTHOR INFORMATION

Corresponding Author

Anju Gupta − *Department of Mechanical, Industrial and Manufacturing Engineering, The University of Toledo, Toledo, Ohio 43606, United States;* ● orcid.org/0000-0001-5378-9496; Phone: +1 (413) 530-8213; Email: anju.gupta@utoledo.edu

Authors

Saketh Merugu − *Department of Mechanical, Industrial and Manufacturing Engineering, The University of Toledo, Toledo, Ohio 43606, United States*

Logan T. Kearney − *Carbon and Composites Group, Chemical Sciences Division, Oak Ridge National Laboratory, Oak Ridge, Tennessee 37830, United States*

Jong K. Keum − *Center for Nanophase Materials Science, Oak Ridge National Laboratory, Oak Ridge, Tennessee 37830, United States*

Amit K. Naskar − *Carbon and Composites Group, Chemical Sciences Division, Oak Ridge National Laboratory, Oak Ridge, Tennessee 37830, United States;* ● orcid.org/0000-0002-1094-0325

Jamal Ansary − *Department of Mechanical, Industrial and Manufacturing Engineering, The University of Toledo, Toledo, Ohio 43606, United States*

Aidan Herbert − *DigiM Solution LLC, Woburn, Massachusetts 01801, United States*

Monsur Islam − *IMDEA Materials Institute, Getafe, Madrid 28906, Spain*

Kunal Mondal − *Nuclear Energy and Fuel Cycle Division, Oak Ridge National Laboratory, Oak Ridge, Tennessee 37830, United States;* ● orcid.org/0000-0003-1665-7755

Complete contact information is available at:
https://pubs.acs.org/10.1021/acsomega.4c03024

Author Contributions

Saketh Merugu: Data curation, Formal Analysis, Investigation, Methodology, Validation, Visualization, Writing—original draft, and Writing—Review and Editing, Logan T. Kearney: Investigation, Data curation, and Writing—Review and Editing, Jong K. Keum: Investigation, Amit K. Naskar: Funding acquisition, Resources, and Review and Editing, Aidan Herbert: Software and Methodology, Jamal Ansary: Investigation and Methodology, Monsur Islam: Resources, Kunal Mondal: Resources, Anju Gupta: Funding acquisition, Conceptualization, Project administration, Supervision, and Writing—review and editing.

Notes

The authors declare no competing financial interest.

REFERENCES

(1) Musie, W.; Gonfa, G. Fresh water resource, scarcity, water salinity challenges and possible remedies: a review. *Heliyon* **2023**, *9* (8), No. e18685.

(2) Jones, E.; Qadir, M.; van Vliet, M. T.; Smakhtin, V.; Kang, S.-m. The state of desalination and brine production: a global outlook. *Sci. Total Environ.* **2019**, *657*, 1343−1356.

(3) Deshmukh, S. Ultrapure water production. In *Handbook of Water and Used Water Purification*; Lahnsteiner, J., Ed.; Springer International Publishing, 2020; pp 1−22.

(4) Greenlee, L. F.; Lawler, D. F.; Freeman, B. D.; Marrot, B.; Moulin, P. Reverse osmosis desalination: water sources, technology, and today's challenges. *Water Res.* **2009**, *43* (9), 2317−2348.

(5) Mohammad, A. W.; Teow, Y.; Ang, W.; Chung, Y.; Oatley-Radcliffe, D.; Hilal, N. Nanofiltration membranes review: recent advances and future prospects. *Desalination* **2015**, *356*, 226−254.

(6) Prajapati, M.; Shah, M.; Soni, B. A comprehensive review of the geothermal integrated multi-effect distillation (MED) desalination and its advancements. *Groundw. Sustain. Dev.* **2022**, *19*, 100808.

(7) Al-Amshawee, S.; Yunus, M. Y. B. M.; Azoddein, A. A. M.; Hassell, D. G.; Dakhil, I. H.; Hasan, H. A. Electrodialysis desalination for water and wastewater: a review. *Chem. Eng. J.* **2020**, *380*, 122231.

(8) Li, Y.; Thomas, E. R.; Molina, M. H.; Mann, S.; Walker, W. S.; Lind, M. L.; Perreault, F. Desalination by membrane pervaporation: a review. *Desalination* **2023**, *547*, 116223.

(9) Guan, G.; Yao, C.; Lu, S.; Jiang, Y.; Yu, H.; Yang, X. Sustainable operation of membrane distillation for hypersaline applications: roles of brine salinity, membrane permeability and hydrodynamics. *Desalination* **2018**, *445*, 123−137.

(10) Yadav, A.; Labhasetwar, P. K.; Shahi, V. K. Membrane distillation using low-grade energy for desalination: a review. *J. Environ. Chem. Eng.* **2021**, *9* (5), 105818.

(11) Kalla, S.; Piash, K. S.; Sanyal, O. Anti-fouling and anti-wetting membranes for membrane distillation. *J. Water Process Eng.* **2022**, *46*, 102634.

(12) Kaczmarczyk, M.; Mukti, M.; Ghaffour, N.; Soukane, S.; Bundschuh, J.; Tomaszewska, B. Renewable energy-driven membrane distillation in the context of life cycle assessment. *Renew. Sustain. Energy Rev.* **2024**, *192*, 114249.

(13) Felix, V.; Hardikar, M.; Hickenbottom, K. L. Concentrate circularity: a comparative techno-economic analysis of membrane distillation and conventional inland concentrate management technologies. *Desalination* **2024**, *574*, 117213.

(14) Tai, Z. S.; Othman, M. H. D.; Koo, K. N.; Mustapa, W. N. F. W.; Kadirkhan, F. Membrane innovations to tackle challenges related to flux, energy efficiency and wetting in membrane distillation: a state-of-the-art review. *Sustainable Mater. Technol.* **2024**, *39*, No. e00780.

(15) Lawson, K. W.; Lloyd, D. R. Membrane distillation. *J. Membr. Sci.* **1997**, *124* (1), 1−25.

(16) Tan, G. M.; Xu, D.; Zhu, Z. G.; Zhang, X.; Li, J. S. Tailoring pore size and interface of superhydrophobic nanofibrous membrane for robust scaling resistance and flux enhancement in membrane distillation. *J. Membr. Sci.* **2022**, *658*, 120751.

(17) Deshmukh, A.; Elimelech, M. Understanding the impact of membrane properties and transport phenomena on the energetic performance of membrane distillation desalination. *J. Membr. Sci.* **2017**, *539*, 458−474.

(18) Swaminathan, J.; Chung, H. W.; Warsinger, D. M.; Lienhard V, J. H. Energy efficiency of membrane distillation up to high salinity: evaluating critical system size and optimal membrane thickness. *Appl. Energy* **2018**, *211*, 715−734.

(19) Zuo, J.; Chung, T. S.; O'Brien, G. S.; Kosar, W. Hydrophobic/hydrophilic PVDF/Ultem dual-layer hollow fiber membranes with enhanced mechanical properties for vacuum membrane distillation. *J. Membr. Sci.* **2017**, *523*, 103−110.

(20) Rishi, A. M.; Gupta, A.; Kandlikar, S. G. Improving aging performance of electrodeposited copper coatings during pool boiling. *Appl. Therm. Eng.* **2018**, *140*, 406−414.

(21) Rishi, A. M.; Kandlikar, S. G.; Gupta, A. Improved wettability of graphene nanoplatelets (GNP)/copper porous coatings for dramatic improvements in pool boiling heat transfer. *Int. J. Heat Mass Transfer* **2019**, *132*, 462−472.

(22) Lin, J. Y.; Du, J. L.; Xie, S. L.; Yu, F.; Fang, S. Q.; Yan, Z. S.; Lin, X. C.; Zou, D.; Xie, M.; Ye, W. Y. Durable superhydrophobic polyvinylidene fluoride membranes via facile spray-coating for effective membrane distillation. *Desalination* **2022**, *538*, 115925.

(23) Rishi, A. M.; Kandlikar, S. G.; Gupta, A. Salt templated and graphene nanoplatelets draped copper (GNP-draped-Cu) composites for dramatic improvements in pool boiling heat transfer. *Sci. Rep.* **2020**, *10* (1), 11941.

(24) Rishi, A. M.; Kandlikar, S. G.; Rozati, S. A.; Gupta, A. Effect of ball milled and sintered graphene nanoplatelets-copper composite coatings on bubble dynamics and pool boiling heat transfer. *Adv. Eng. Mater.* **2020**, *22* (7), 1901562.

(25) Gupta, A. Repetitive pool boiling tests: controlled process to form reduced GO surfaces from GO with tunable surface chemistry and morphology. In *Abstracts of Papers of the American Chemical Society*; American Chemical Society: 1155 16th st, NW, Washington, DC 20036 USA, 2019; Vol. *258*.

(26) Rao, C.; Biswas, K.; Subrahmanyam, K.; Govindaraj, A. Graphene, the new nanocarbon. *J. Mater. Chem.* **2009**, *19* (17), 2457−2469.

(27) Compton, O. C.; Nguyen, S. T. Graphene oxide, highly reduced graphene oxide, and graphene: versatile building blocks for carbon-based materials. *Small* **2010**, *6* (6), 711−723.

(28) Tarcan, R.; Todor-Boer, O.; Petrovai, I.; Leordean, C.; Astilean, S.; Botiz, I. Reduced graphene oxide today. *J. Mater. Chem. C* **2020**, *8* (4), 1198−1224.

(29) Jang, B. Z.; Zhamu, A. Processing of nanographene platelets (NGPs) and NGP nanocomposites: a review. *J. Mater. Sci.* **2008**, *43* (15), 5092−5101.

(30) Rao, Z.; Wen, Y.; Liu, C. Enhancement of heat transfer of microcapsulated particles using copper particles and copper foam. *Particuology* **2018**, *41*, 85−93.

(31) Gupta, A.; Jaikumar, A.; Kandlikar, S. G.; Rishi, A.; Layman, A. A multiscale morphological insight into graphene based coatings for pool boiling applications. *Heat Transfer Eng.* **2018**, *39* (15), 1331−1343.

(32) Sawant, S. R.; Kalla, S.; Murthy, Z. V. P. Enhanced properties of the PVDF membrane with carboxylated MWCNT and sodium alginate for membrane distillation. *J. Environ. Chem. Eng.* **2023**, *11* (2), 109259.

(33) Wei, Z. Z.; Jin, Y.; Li, J.; Jia, L. Y.; Ma, Y. J.; Chen, M. Preparation of superhydrophobic PVDF composite membrane via catechol/polyamine co-deposition and Ag nanoparticles in-situ growth for membrane distillation. *Desalination* **2022**, *529*, 115649.

(34) Reddy, A. S.; Kalla, S.; Murthy, Z. V. P. Nano-particles enhanced hydrophobic membranes: high-performance study for dye wastewater treatment using membrane distillation. *J. Water Process Eng.* **2022**, *46*, 102610.

(35) Yadav, P.; Farnood, R.; Kumar, V. Superhydrophobic modification of electrospun nanofibrous Si@PVDF membranes for desalination application in vacuum membrane distillation. *Chemosphere* **2022**, *287* (Pt 2), 132092.

(36) Hui Ting, L. L.; Teow, Y. H.; Mahmoudi, E.; Ooi, B. S. Development and optimization of low surface free energy of rGO-PVDF mixed matrix membrane for membrane distillation. *Sep. Purif. Technol.* **2023**, *305*, 122428.

(37) Xie, B. L.; Xu, G. R.; Jia, Y. H.; Gu, L. K.; Wang, Q.; Mushtaq, N.; Cheng, B. W.; Hu, Y. X. Engineering carbon nanotubes enhanced hydrophobic membranes with high performance in membrane distillation by spray coating. *J. Membr. Sci.* **2021**, *625*, 118978.

(38) Tibi, F.; Park, S. J.; Kim, J. Improvement of membrane distillation using PVDF membrane incorporated with TiO(2)

modified by silane and optimization of fabricating conditions. *Membranes* **2021**, *11* (2), 95.

(39) Fomin, S.; Shirokova, E.; Kraeva, I.; Tolstobrov, I.; Bushuev, A.; Yuzhanin, K.; Ananchenko, B.; Vetcher, A. A.; Iordanskii, A. Effect of polyvinylidene fluoride membrane production conditions on its structure and performance characteristics. *Polymers* **2022**, *14* (23), 5283.

(40) Koseki, Y.; Aimi, K.; Ando, S. Crystalline structure and molecular mobility of PVDF chains in PVDF/PMMA blend films analyzed by solid-state 19F MAS NMR spectroscopy. *Polym. J.* **2012**, *44* (8), 757−763.

(41) Liu, J.; Lu, X.; Wu, C. Effect of preparation methods on crystallization behavior and tensile strength of poly (vinylidene fluoride) membranes. *Membranes* **2013**, *3* (4), 389−405.

(42) Ruan, L.; Yao, X.; Chang, Y.; Zhou, L.; Qin, G.; Zhang, X. Properties and applications of the β phase poly(vinylidene fluoride). *Polymers* **2018**, *10* (3), 228.

(43) Indolia, A. P.; Gaur, M. Investigation of structural and thermal characteristics of PVDF/ZnO nanocomposites. *J. Therm. Anal. Calorim.* **2013**, *113* (2), 821−830.

(44) Saxena, P.; Shukla, P.; Gaur, M. Thermal analysis of polymer blends and double layer by DSC. *Polym. Polym. Compos.* **2021**, *29* (9_suppl), S11−S18.

(45) Qi-lin, X.; Xin, T. Effect of polymer matrix and nanofiller on non-bonding interfacial properties of nanocomposites. *J. Polym. Res.* **2017**, *24*, 15.

(46) Sarfraz, M. Carbon capture via mixed-matrix membranes containing nanomaterials and metal-organic frameworks. *Membr. Environ. Appl.* **2020**, *42*, 45−94.

(47) Muntha, S. T.; Siddiq, M.; Kausar, A.; Khan, A. Mixed matrix membranes of polysulfone/polyimide reinforced with modified zeolite based filler: preparation, properties and application. *Chin. J. Polym. Sci.* **2018**, *36* (1), 65−77.

(48) Tadros, T. Flory-Huggins interaction parameter. In *Encyclopedia of Colloid and Interface Science*; Tadros, T., Ed.; Springer: Berlin/Heidelberg, Germany, 2013; pp 523−524..

(49) Xavier, P.; Rao, P.; Bose, S. Nanoparticle induced miscibility in LCST polymer blends: critically assessing the enthalpic and entropic effects. *Phys. Chem. Chem. Phys.* **2016**, *18* (1), 47−64.

(50) Patel, R. K.; Jonnalagadda, S.; Gupta, P. K. Use of Flory-Huggins interaction parameter and contact angle values to predict the suitability of the drug-polymer system for the production and stability of nanosuspensions. *Pharm. Res.* **2022**, *39* (5), 1001−1017.

(51) Leaper, S.; Abdel-Karim, A.; Faki, B.; Luque-Alled, J. M.; Alberto, M.; Vijayaraghavan, A.; Holmes, S. M.; Szekely, G.; Badawy, M. I.; Shokri, N.; et al. Flux-enhanced PVDF mixed matrix membranes incorporating APTS-functionalized graphene oxide for membrane distillation. *J. Membr. Sci.* **2018**, *554*, 309−323.

(52) Grakovich, P. N.; Allayarov, S. R.; Confer, M. P.; Kalinin, L. A.; Frolov, I. A.; Rudneva, T. N.; Ivanov, L. F.; Dixon, D. A. Infrared laser ablation of poly (vinylidene fluoride): the loss of HF. *J. Fluorine Chem.* **2022**, *255−256*, 109947.

(53) Wongchitphimon, S.; Lee, S. S.; Chuah, C. Y.; Wang, R.; Bae, T. H. Composite materials for carbon capture. In *Materials for Carbon Capture*; Wiley, 2020; pp 237−266..

(54) Yuan, X. T.; Xu, C. X.; Geng, H. Z.; Ji, Q.; Wang, L.; He, B.; Jiang, Y.; Kong, J.; Li, J. Multifunctional PVDF/CNT/GO mixed matrix membranes for ultrafiltration and fouling detection. *J. Hazard. Mater.* **2020**, *384*, 120978.

(55) Wang, T.; Chen, Z.; Gong, W.; Xu, F.; Song, X.; He, X.; Fan, M. Electrospun carbon nanofibers and their applications in several areas. *ACS Omega* **2023**, *8* (25), 22316−22330.

(56) Hosseini, S. M.; Moradi, F.; Farahani, S. K.; Bandehali, S.; Parvizian, F.; Ebrahimi, M.; Shen, J. Carbon nanofibers/chitosan nanocomposite thin film for surface modification of poly (ether sulphone) nanofiltration membrane. *Mater. Chem. Phys.* **2021**, *269*, 124720.

(57) Yan, J.; Dong, K.; Zhang, Y.; Wang, X.; Aboalhassan, A. A.; Yu, J.; Ding, B. Multifunctional flexible membranes from sponge-like

porous carbon nanofibers with high conductivity. *Nat. Commun.* **2019**, *10* (1), 5584.

(58) Zhang, W.-m.; Yan, J.; Su, Q.; Han, J.; Gao, J.-f. Hydrophobic and porous carbon nanofiber membrane for high performance solar-driven interfacial evaporation with excellent salt resistance. *J. Colloid Interface Sci.* **2022**, *612*, 66−75.

(59) Kocjan, A.; Logar, M.; Shen, Z. The agglomeration, coalescence and sliding of nanoparticles, leading to the rapid sintering of zirconia nanoceramics. *Sci. Rep.* **2017**, *7* (1), 2541.

(60) Husna, A.; Hossain, I.; Choi, O.; Lee, S. M.; Kim, T. H. Efficient CO2 separation using a PIM-PI-functionalized UiO-66 MOF incorporated mixed matrix membrane in a PIM-PI-1 polymer. *Macromol. Mater. Eng.* **2021**, *306* (10), 2100298.

(61) Park, S.; Jeong, H.-K. In-situ linker doping as an effective means to tune zeolitic-imidazolate framework-8 (ZIF-8) fillers in mixed-matrix membranes for propylene/propane separation. *J. Membr. Sci.* **2020**, *596*, 117689.

(62) Michaels, A. S. Analysis and prediction of sieving curves for ultrafiltration membranes: A universal correlation? *Sep. Sci. Technol.* **1980**, *15* (6), 1305−1322.

(63) Wei, Y.; Chu, H. Q.; Dong, B. Z.; Li, X.; Xia, S. J.; Qiang, Z. M. Effect of TiO$_2$ nanowire addition on PVDF ultrafiltration membrane performance. *Desalination* **2011**, *272* (1−3), 90−97.

(64) Quéré, D. Wetting and roughness. *Annu. Rev. Mater. Res.* **2008**, *38*, 71−99.

(65) Ansari, A.; Galogahi, F. M.; Thiel, D. V.; Helfer, F.; Millar, G.; Soukane, S.; Ghaffour, N. Downstream variations of air-gap membrane distillation and comparative study with direct contact membrane distillation: a modelling approach. *Desalination* **2022**, *526*, 115539.

(66) Zuo, J.; Bonyadi, S.; Chung, T. S. Exploring the potential of commercial polyethylene membranes for desalination by membrane distillation. *J. Membr. Sci.* **2016**, *497*, 239−247.

(67) Islam, M.; Dolle, C.; Sadaf, A.; Weidler, P. G.; Sharma, B.; Eggeler, Y. M.; Mager, D.; Korvink, J. G. Electrospun carbon nanofibre-assisted patterning of metal oxide nanostructures. *Microsyst. Nanoeng.* **2022**, *8* (1), 71.

(68) Bajaj, B.; Joh, H. I.; Jo, S. M.; Kaur, G.; Sharma, A.; Tomar, M.; Gupta, V.; Lee, S. Controllable one step copper coating on carbon nanofibers for flexible cholesterol biosensor substrates. *J. Mater. Chem. B* **2016**, *4* (2), 229−236.

(69) Zhang, S.; Byrnes, A. P.; Jankovic, J.; Neilly, J. Management, analysis, and simulation of micrographs with cloud computing. *Microsc. Today* **2019**, *27* (2), 26−33.